Real-World Light Field Image Super-Resolution Via Degradation Modulation

Yingqian Wang, Zhengyu Liang, Longguang Wang, Jungang Yang, Wei An, and Yulan Guo, *Senior Member, IEEE*

***Abstract*— Recent years have witnessed the great advances of deep neural networks (DNNs) in light field (LF) image super-resolution (SR). However, existing DNN-based LF image SR methods are developed on a single fixed degradation (e.g., bicubic downsampling), and thus cannot be applied to super-resolve real LF images with diverse degradation. In this article, we propose a simple yet effective method for real-world LF image SR. In our method, a practical LF degradation model is developed to formulate the degradation process of real LF images. Then, a convolutional neural network is designed to incorporate the degradation prior into the SR process. By training on LF images using our formulated degradation, our network can learn to modulate different degradation while incorporating both spatial and angular information in LF images. Extensive experiments on both synthetically degraded and real-world LF images demonstrate the effectiveness of our method. Compared with existing state-of-the-art single and LF image SR methods, our method achieves superior SR performance under a wide range of degradation, and generalizes better to real LF images. Codes and models are available at https://yingqianwang.github.io/LF-DMnet/.**

***Index Terms*— Degradation modulation, dynamic convolution, image super-resolution (SR), light field (LF).**

I. Introduction

LIGHT field (LF) cameras record both intensity and direction of light rays, and enable many applications such as refocusing [1], depth estimation [2], [3], [4], and view rendering [5], [6], [7]. Since high-resolution (HR) LF images are beneficial to various applications but are generally obtained at an expensive cost, it is necessary to reconstruct HR LF images from low-resolution (LR) LF images, i.e., to achieve LF image super-resolution (SR).

In the past decade, deep neural networks (DNNs) have been successfully applied to LF image SR and achieved significant progress [8], [9], [10], [11], [12]. In the area of LF image SR, many networks [13], [14], [15], [16], [17], [18], [19], [20], [21], [22], [23], [24], [25], [26], [27], [28], [29], [30] were developed to improve SR accuracy. However, real-world LF image SR has remained under investigated due to the following two reasons. First, it is challenging to develop an LF image SR model that can handle real-world degradation. Real-world LF images suffer from diverse degradation which varies with both imaging devices (e.g., Lytro or RayTrix cameras) and shot conditions (e.g., scene depth, focal length, and illuminance). However, existing LF image SR methods focus on the design of network architecture, and develop models on the simple bicubic downsampling degradation. Consequently, these methods suffer a notable performance drop when applied to real LF images. Second, it is challenging to simultaneously utilize the degradation information while incorporating the complementary angular information. Existing methods generally achieve real-world SR on single images (i.e., ignore the view-wise correlation), and thus cannot achieve satisfactory performance on LF image SR.

In this article, we propose a simple yet effective method for real-world LF image SR. In our method, we first formulate

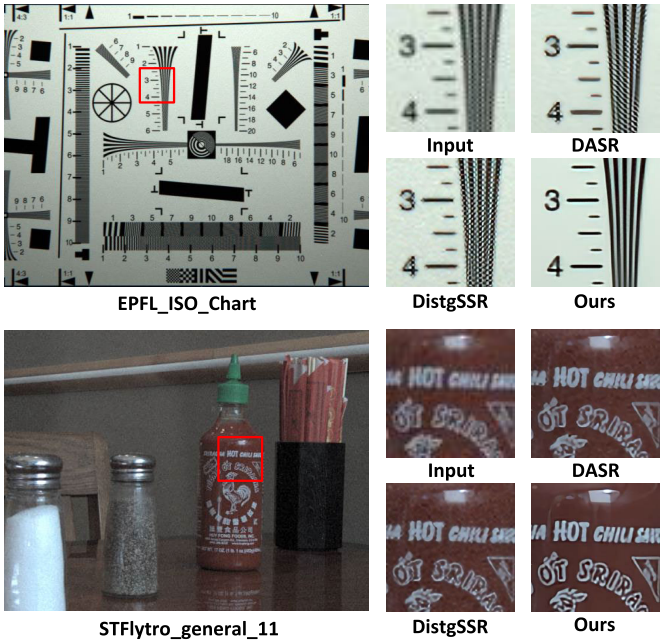

Fig. 1. Visual results achieved by DASR [31], DistgSSR [27], and our method on real LF images for 4 × SR. Scenes *ISO_Chart* from the EPFL dataset [32] and *general_11* from the STFlytro dataset [33] are used for comparison.

Manuscript received 22 December 2022; revised 30 November 2023; accepted 13 March 2024. This work was supported in part by the National Key Research and Development Program of China under Grant 2021YFB3100800, in part by the Outstanding Youth Foundation in Hunan Province under Grant 2024JJ2063, and in part by the National Natural Science Foundation of China under Grant U20A20185, Grant 61972435, and Grant 61921001. *(Corresponding author: Jungang Yang.)*

Yingqian Wang, Zhengyu Liang, Jungang Yang, Wei An, and Yulan Guo are with the College of Electronic Science and Technology, National University of Defense Technology, Changsha 410073, China (e-mail: yangjungang@nudt.edu.cn).

Longguang Wang is with the College of Electronic Science, Aviation University of Air Force, Changchun 130012, China.

Digital Object Identifier 10.1109/TNNLS.2024.3378420

a practical degradation model to approximate the degradation process of real LF images, and then develop a convolutional neural network to super-resolve LF images with diverse and real degradation. To incorporate the degradation prior into the SR process, we design a degradation-modulating convolution (DM-Conv) whose weights are dynamically generated according to the degradation representation. By integrating the proposed DM-Conv with the disentangling mechanism [27], our network (namely, LF-DMnet) can well incorporate spatial and angular information under diverse degradation. As shown in Fig. 1, compared with DistgSSR [27] and DASR [31], our method achieves better performance on real LF images and generates images with more clear details and fewer artifacts.

The contributions of this work are summarized as follows.

1) We propose a practical LF degradation model to handle the real-world LF image SR problem. Different from existing works which focus on the advanced network designs, we first address the importance of degradation formulation and modulation in LF image SR.
2) We propose a degradation-modulating network (i.e., LF-DMnet) to incorporate the degradation prior into the SR process. Extensive ablation studies and model analyses validate the effectiveness of our degradation modulation mechanism.
3) Our method achieves state-of-the-art SR performance on both synthetic and real-world degradation, which not only provides a simple yet strong baseline, but also takes a step toward practical real-world LF image SR.

The rest of this article is organized as follows. In Section II, we briefly review the related works. In Section III, we describe our degradation model for LF image SR. In Section IV, we introduce the details and design thoughts of our LF-DMnet. Experimental results are presented in Section V. Finally, we conclude this article in Section VI.

II. Related Work

In this section, we briefly review several major works for DNN-based single image SR and LF image SR.

A. Single Image Super-Resolution

The goal of single image SR is to reconstruct an HR image from its LR version. According to different degradation settings, existing single image SR methods can be roughly categorized to single degradation-based methods and multidegradation-based methods.

Early works on DNN-based single image SR are generally developed on a single and fixed degradation (e.g., bicubic downsampling). Dong et al. [34] first applied convolution neural networks to image SR and developed a three-layer network named SRCNN. Although SRCNN is shallow and lightweight, it outperforms many traditional SR methods [35], [36], [37], [38]. Since then, deep networks have dominated the SR area and achieved continuously improved accuracy with large models and complex architectures. Kim et al. [39] applied global residual learning strategy to image SR and developed a 20-layer network called VDSR. Lim et al. [40] proposed an enhanced deep SR (EDSR) network by using both global and local residual connections. Zhang et al. [41] combined residual learning with dense connection to build a residual dense network with more than 100 layers. Subsequently, Zhang et al. [42] developed a very deep network in a residual-in-residual architecture to achieve competitive SR accuracy. More recently, attention mechanism [43], [44], [45] and Transformer architectures [46], [47] have been extensively studied to achieve state-of-the-art SR performance.

Although the aforementioned methods have achieved continuously improved SR performance, they are designed for a single fixed degradation (e.g., bicubic downsampling) and will suffer from a significant performance drop when the degradation differs from the assumed one. Consequently, many methods have been proposed to achieve image SR with multiple various degradation [48]. Zhang et al. [49] proposed an SRMD network where the degradation map was concatenated with the LR image as the input of the DNN. Subsequently, Xu et al. [50] applied dynamic convolutions to achieve better SR performance than SRMD. In [51], an unfolding SR network was developed to handle different degradation by alternately solving a data subproblem and a prior subproblem. Gu et al. [52] proposed an iterative kernel correction method (namely, IKC) to correct the estimated degradation by observing previous SR results. More recently, Wang et al. [31] achieved degradation representation learning in a contrastive manner and developed a degradation-aware SR network named DASR for real-world single image SR.

B. LF Image Super-Resolution

The goal of LF image SR is to super-resolve each subaperture image (SAI) of an LF. A straightforward scheme to achieve LF image SR is applying single image SR methods to each SAI independently. However, this scheme cannot achieve a good performance since the complementary angular information among different views is not considered. Consequently, existing LF image SR methods focus on designing advanced network architectures to fully use both spatial and angular information.

Yoon et al. [13] proposed the first DNN-based method called LFCNN to enhance both spatial and angular resolution of an LF. In their method, SAIs are first super-resolved using SRCNN [34], and then finetuned in pairs or quads to incorporate angular information. Wang et al. [15] proposed a bidirectional recurrent network for LF image SR, in which the angular information in adjacent horizontal and vertical views was incorporated in a recurrent manner. Zhang et al. [19] proposed a multibranch residual network to incorporate the multidirectional epipolar geometry prior for LF image SR. In their subsequent work MEG-Net [23], the SR performance was further improved by applying 3-D convolutions to SAI stacks of different angular directions. Jin et al. [20] developed an all-to-one method for LF image SR, and performed structural consistency regularization to preserve the LF parallax structure. Wang et al. [21] developed an LF-InterNet to repetitively interact spatial and angular information for LF image SR, and then generalized the spatial-angular interaction

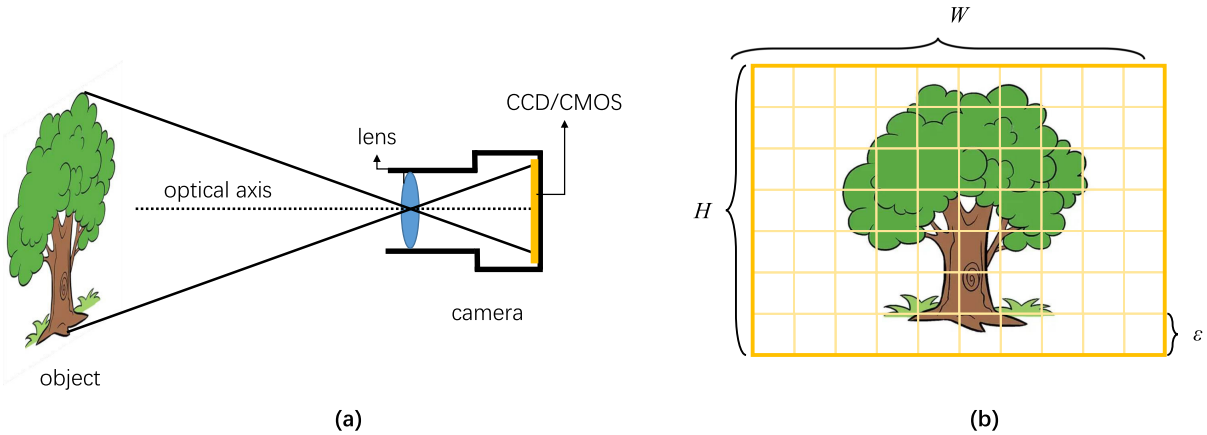

Fig. 2. Illustration of the camera imaging process. (a) Camera imaging model. (b) Image on the sensors.

mechanism to the disentangling mechanism [27] to achieve state-of-the-art SR accuracy.

More recently, Wang et al. [22] used deformable convolutions [53], [54] to address the disparity problem in LF image SR. Cheng et al. [24] proposed a zero-shot learning scheme to handle the domain gap among different LF datasets. Liang et al. [29] proposed a Transformer-based LF image SR network, in which a spatial Transformer and an angular Transformer were designed to model long range spatial dependencies and angular correlation, respectively. Wang et al. [28] proposed a detail-preserving Transformer to exploit nonlocal context information and preserve details for LF image SR. Heber et al. [30] investigated the nonlocal spatial-angular correlations in LF image SR, and developed a Transformer-based network called EPIT to achieve state-of-the-art SR performance.

Although remarkable progress have been achieved in LF image SR, existing methods only focus on the advanced network design but ignored the generalization capability to real-world degradation. In this article, we handle the real-world LF image SR problem by formulating a practical LF degradation model and designing a degradation-modulating network.

III. LF Image Degradation Formulation

In this section, we formulate a general and practical degradation model for real-world LF image SR. In Section III-A, we analyze the camera imaging process and derive the image degradation model. In Section III-B, we extend the degradation model to 4-D LF images to build the LF image degradation model, and discuss its key components. In Section III-C, we compare the differences between our method and existing SR methods.

A. Degradation Formulation

In this section, we first formulate the camera imaging process considering three key factors including *point spread function* (PSF), *sensor sampling*, and *additional noise*. Then, we derive the image degradation model based on the formulated camera imaging process.

Fig. 2 shows a toy example of the camera imaging process, in which the light rays are first projected onto the sensor plane [as shown in Fig. 2(a)], and then sampled by the sensor units [as shown in Fig. 2(b)]. Let $\mathcal{I}_{\text{real}} : (x, y) \rightarrow \mathbb{R}$ be the real image (a 2-D continuous function) on the sensor plane, k_{psf} be the PSF of the camera imaging system,[1] $\mathcal{I}_{\text{ideal}} : (x, y) \rightarrow \mathbb{R}$ be the "ideal" image (a 2-D continuous function) without considering the point spread process. According to the camera imaging process, the "real" image is obtained by convolving the "ideal" image with the PSF, i.e.,

$$\mathcal{I}_{\text{real}}(x, y) = \int_{-\infty}^{+\infty} \int_{-\infty}^{+\infty} k_{\text{psf}}(u, v) \cdot \mathcal{I}_{\text{ideal}}(x - u, y - v)\, du dv \quad (1)$$

which can be denoted as

$$\mathcal{I}_{\text{real}} = \mathcal{I}_{\text{ideal}} \otimes k_{\text{psf}} \quad (2)$$

where $\otimes$ represents the convolution operation. Assume that the size of each sensor unit is $\epsilon \times \epsilon$, the sampling process on the sensor unit (h, w) can be formulated as

$$\mathcal{I}_{\text{LR}}(h, w) = \int_{h-\frac{\epsilon}{2}}^{h+\frac{\epsilon}{2}} \int_{w-\frac{\epsilon}{2}}^{w+\frac{\epsilon}{2}} \mathcal{I}_{\text{real}}(x, y) dx dy + \mathcal{N}(h, w) \quad (3)$$

where $\mathcal{I}_{\text{LR}} \in \mathbb{R}^{H \times W}$ is the output of the sensor (i.e., a digital image). Here, we introduce $[\cdot]_\epsilon$ to denote the sampling process with a sampling grid of $\epsilon \times \epsilon$. Then, (3) can be rewritten as

$$\mathcal{I}_{\text{LR}} = [\mathcal{I}_{\text{real}}]_\epsilon + \mathcal{N} \quad (4)$$

where $\mathcal{N} \in \mathbb{R}^{H \times W}$ represents random noise in the imaging process.

In image SR task, it is expected to reconstruct (or estimate) the ideal image function $\mathcal{I}_{\text{ideal}}$ from the observed LR image $\mathcal{I}_{\text{LR}}$. Since continuous 2-D image function needs to be presented via a digital image, we further introduce HR image $\mathcal{I}_{\text{HR}} \in \mathbb{R}^{\alpha H \times \alpha W}$ to quantize $\mathcal{I}_{\text{ideal}}$, i.e.,

$$\mathcal{I}_{\text{HR}} = [\mathcal{I}_{\text{ideal}}]_{\frac{\epsilon}{\alpha}} \quad (5)$$

where α is defined as the upsampling factor. From (5), we can consider that the HR image is obtained by sampling the

[1] According to the signal processing theory, PSF can be considered as the *unit impulse response* of the camera imaging system.

ideal image $\mathcal{I}_{\text{ideal}}$ with smaller interval $(\epsilon/\alpha) \times (\epsilon/\alpha)$. Here, we introduce a downsampling operator $(\cdot)_{\downarrow_\alpha}$ to build the relationship between LR image and its HR version, i.e.,

$$[\mathcal{I}]_\epsilon = \left([\mathcal{I}]_{\frac{\epsilon}{\alpha}}\right)_{\downarrow_\alpha}, \quad \mathcal{I} = \mathcal{I}_{\text{ideal}} \text{ or } \mathcal{I}_{\text{real}}. \tag{6}$$

Substitute (2) and (6) into (4), we can obtain

$$\mathcal{I}_{\text{LR}} = \left(\left[\mathcal{I}_{\text{ideal}} \otimes k_{\text{psf}}\right]_{\frac{\epsilon}{\alpha}}\right)_{\downarrow_\alpha} + \mathcal{N}. \tag{7}$$

According to the *commutative law of convolution and sampling* (see Appendix[2] for prove), there is

$$\left[\mathcal{I}_{\text{ideal}} \otimes k_{\text{psf}}\right]_{\frac{\epsilon}{\alpha}} = [\mathcal{I}_{\text{ideal}}]_{\frac{\epsilon}{\alpha}} \otimes k_{\text{psf}}. \tag{8}$$

When we substitute (8) into (7), we can obtain the image degradation model as

$$\mathcal{I}_{\text{LR}} = (\mathcal{I}_{\text{HR}} \otimes k)_{\downarrow_\alpha} + \mathcal{N}. \tag{9}$$

The above degradation model can be considered as a process in which the real observed LR image is obtained by blurring, downsampling and adding noise on the HR image. In Section III-B, we will apply the degradation model to 4-D LFs to formulate our LF image degradation model.

B. LF Image Degradation Model

We use the two-plane model [55] to parameterize 4-D LF as $\mathcal{L} \in \mathbb{R}^{U \times V \times H \times W}$, where U and V represent angular dimensions, H and W represent spatial dimensions. Since this article focuses on enhancing the spatial resolution of LFs, we use the SAI representation in [27] to describe our method. That is, an LF can be considered as a $U \times V$ array of SAIs, and each SAI has a spatial size of $H \times W$.

Here, we extend our degradation model [i.e., (9)] to 4-D LFs and build the LF image degradation model as

$$\mathcal{I}^{lr}_{u,v} = \left(\mathcal{I}^{hr}_{u,v} \otimes k_{u,v}\right)\downarrow_\alpha + \mathcal{N}_{u,v} \tag{10}$$

where $\mathcal{I}^{lr}_{u,v} \in \mathbb{R}^{H \times W \times 3}$ denotes the input LR SAI of view (u, v), and $\mathcal{I}^{hr}_{u,v} \in \mathbb{R}^{\alpha H \times \alpha W \times 3}$ denotes the corresponding HR SAI. $k_{u,v} \in \mathbb{R}^{21 \times 21}$ and $\mathcal{N}_{u,v} \in \mathbb{R}^{H \times W \times 3}$ represent the blur kernel and additional noise of view (u, v), respectively. In the following text, we introduce the details of the three key components (i.e., blur kernel, noise, and downsamping) of our LF image degradation model.

1) Blur Kernel: We follow existing works [49], [52] to use the isotropic Gaussian kernel parameterized by kernel width to synthesize blurring LF images. Note that, although anisotropic kernels (e.g., anisotropic Gaussian blur and motion blur) are also used in recent single image SR methods [31], [51], [56], [57], [58] for degradation modeling, we do not consider these blur kernels in our method because under LF structures, the rotation angle of the anisotropic Gaussian kernel and the trajectory of the motion blur of each SAI should be different but correlated. The formulation of these anisotropic blur kernels depends on the 6-D pose changing of LF cameras, and belongs to the LF deblurring task [59], [60], [61]. As demonstrated in Section V-B2, based on the isotropic Gaussian blur assumption, our method can achieve promising SR performance on real LF images.

[2]https://yingqianwang.github.io/LF-DMnet/Appendix.pdf

2) Noise: Real-world LF images (especially those captured by Lytro cameras) generally have large noise. Directly super-resolving noisy LF images without performing noise reduction can result in visually unpleasant artifacts (see Section V-D2). In this article, we consider the simple channel-independent additive white Gaussian noise in our degradation process. Each element in the noise tensor $\mathcal{N} \in \mathbb{R}^{H \times W \times 3}$ is a random variable with a mean value of 0 and an adjustable standard deviation (i.e., noise level). It is demonstrated in Section V-D2 that, when the noise term is considered in our degradation model, the super-resolved images are more smooth and clean with less noise residual and ringing artifacts.

3) Downsampling: We adopt the widely used bicubic downsampling approach in our method. In this way, our degradation model can be degeneralized to a standard bicubic downsampling degradation when the kernel width and noise level equal to zero. Note that, different from blur kernel and noise level which can vary in the training phase, the downsampling approach is assumed to be fixed.

C. Comparison to Existing Works

1) Compared to Existing LF Image SR Methods: Compared to existing LF image SR methods [19], [20], [21], [22], [23], [27], [28], [29] which use the bicubic downsampling approach to produce LR LF images, our method adopts a more practical degradation model [i.e., (10)] since the blur kernel and noise level in our model can be adjusted in the training phase to enlarge the degradation space. It is shown in Section V-B2 that our LF-DMnet trained with this degradation model can achieve promising SR performance on real LF images, which demonstrates that our proposed degradation model can well cover the real-world degradation of LF images.

2) Compared to More Complex Synthetic Degradation: It is also worth noting that several recent works for single image SR [62], [63] designed very complex degradation models to train deep networks for real-world SR. In these methods, various kinds of blur, noise, and downsampling schemes were considered, and the order of these degradation elements (also including JPEG compression) were randomly shuffled to cover as much real-world degradation as possible. Although these methods [62], [63] achieve favorable visual performance on real-world images, we do not consider designing such a complex degradation model in this article because of the following three reasons. ***First***, single images are generally captured by various cameras and transmitted multiple times on internet, and thus go through complex and high-order degradation [63]. In contrast, LF images are captured by a few kinds of imaging devices (e.g., Lytro or RayTrix), and saved to specific file formats that do not go through JPEG compression. Consequently, the degradation space of LF images is smaller than that of single images. ***Second***, abundant high-quality HR images and diverse scenarios are required to train a network to fit such complex degradation. Networks in [62] and [63] were trained on multiple large-scale single image datasets [64], [65], [66], [67] with thousands of high-quality HR images. In contrast, publicly available high-quality LF datasets are limited in amount, spatial resolution, and scene diversity.

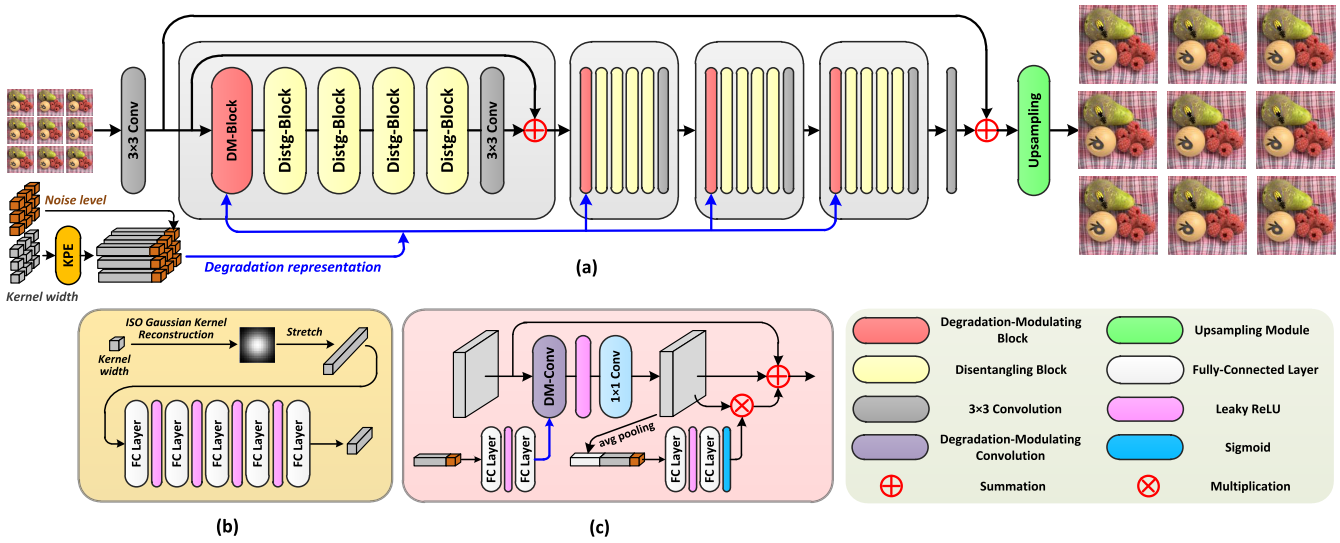

Fig. 3. Overview of our LF-DMnet. (a) Overall architecture. (b) KPE module. (c) DM-block.

Consequently, it is difficult for an LF image SR network to learn such complex degradation with insufficient training samples. ***Third***, as the first work to address LF image SR with multiple degradation, we aim to demonstrate the importance of degradation modulation to LF image SR, and propose a simple yet effective solution to this problem. Consequently, we do not make our degradation model over-complex.

IV. Network Architecture

A. Overview

Based on the degradation model in (10), we develop a degradation-modulating network (LF-DMnet) that can super-resolve LF images with various degradation. An overview of our LF-DMnet is shown in Fig. 3(a). Given an array of LR SAIs and their corresponding degradation (i.e., kernel width and noise level of each view), our LF-DMnet sequentially performs kernel prior embedding (KPE), degradation-modulated feature extraction, and upsampling. Following [27], we build our network by cascading four residual groups. In each residual group, a degradation-modulating block (DM-Block) is designed to process features according to the degradation, and four disentangling blocks (Distg-Blocks) are used to achieve spatial-angular information incorporation. The final output of our network is an array of HR LF images. Note that, since most LF image SR methods [16], [19], [20], [21], [22], [27], [29] use SAIs distributed in a square array as their inputs, in this article, we follow these methods and set $U = V = A$, where A denotes the angular resolution. In the following sections, we will introduce the details of our network design.

B. Kernel Prior Embedding

Handling image SR with multidegradation is more challenging than handling that with bicubic downsampling only, since the solution space of the former one is much larger than the latter one. In such case, incorporating kernel priors into the SR process can constrain the solution space to a mainfold and thus reduce the ill-posedness of the SR process [56]. Since only isotropic Gaussian kernel (with different kernel widths) is considered in our method, we designed a KPE module to fully incorporate the kernel prior into the SR process.

In the KPE module, the isotropic Gaussian kernel $k \in \mathbb{R}^{21\times21}$ is first reconstructed according to the input kernel width (i.e., the only undetermined coefficient). The reconstructed kernel is then stretched into a 1-D tensor $\mathbf{v}_k \in \mathbb{R}^{441\times1}$ and fed to a multilayer perception (MLP) unit with five fully connected (FC) layers to learn the internal characteristics. The output of the MLP is a compact blur representation with reduced dimensionality, i.e., $\mathbf{v}_{\text{blur}} \in \mathbb{R}^{15\times1}$. Finally, the generated blur representation is concatenated with the noise level to produce the final degradation representation $\mathbf{v}_{\text{dg}} \in \mathbb{R}^{16\times1}$. It is demonstrated in Section V-C that the proposed KPE module is beneficial to the SR performance.

C. Degradation-Modulating Block

DM-Block is designed to process image features based on the given degradation. To achieve this goal, a simple and straightforward scheme is to concatenate degradation representation with image features and fuse them via convolutions [49], [50]. However, as demonstrated in several recent works [31], [52], directly convolving image features with degradation representations can cause interference since there is a domain gap between these two kinds of representations. Motivated by the fact that images with different degradation are generated by convolving the original high-quality image using isotropic Gaussian kernel with different kernel widths, in this article, we design a DM-Conv whose kernels are dynamically generated according to the input degradation representation.

Specifically, in each DM-Block, the degradation representation $\mathbf{v}_{\text{dg}}$ is first fed to two FC layers to produce a convolutional kernel $\mathbf{w}$ (with a size of $3 \times 3 \times 64$ in this article). Then, the input feature $\mathcal{F}_{\text{input}}$ is processed with DM-Conv (using $\mathbf{w}$) and another 1×1 convolution to generate $\mathcal{F}^{\text{spa}}_{\text{mod}}$. Note

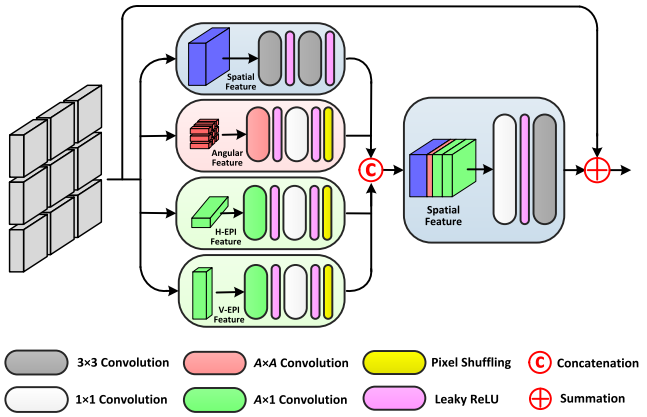

Fig. 4. Architecture of our modified Distg-Block.

that, we follow [31] to design our DM-Conv as a depth-wise dynamic convolution, and use a channel attention layer to reweight the output features based on the statistics of both image feature (produced by performing average pooling on $\mathcal{F}_{\text{mod}}^{\text{spa}}$) and degradation representation. Specifically, the degradation representation $\mathbf{v}_{\text{dg}}$ is passed to another two FC layers and a *Sigmoid* activation layer to generate channel-wise modulation coefficients, which are then used to rescale different channels of $\mathcal{F}_{\text{mod}}^{\text{spa}}$, resulting in $\mathcal{F}_{\text{mod}}$. Finally, $\mathcal{F}_{\text{mod}}$ is summed up with $\mathcal{F}_{\text{input}}$ and $\mathcal{F}_{\text{mod}}^{\text{spa}}$ to produce the output of our DM-Block. It is demonstrated in Section V-C that our method benefits from DM-Conv and degradation-modulating channel attention, and can well handle LF images with various degradation.

D. Disentangling Block

Although the proposed DM-Block can handle input images with various degradation, it processes the image features of different views separately without considering the interview correlation. Since information both within a single view and among different views is beneficial to the performance of LF image SR, in this article, we modify the Distg-Block [27] to incorporate multidimensional information for LF image SR.

Different from the Distg-Block in [27] where a series of specifically designed convolutions (i.e., spatial, angular, and epipolar feature extractors) are applied to a single macropixel image (MacPI) feature, in this article, we organize LF features into different shapes and apply plain convolutions to the reshaped features. Our modified approach is equivalent to the original design but is more simple and generic. Specifically, considering both batch and channel dimensions, the input feature of our Distg-Block can be denoted by $\mathcal{F}_{\text{in}}^{6-D} \in \mathbb{R}^{B\times U\times V\times C\times H\times W}$, where B, C, H, and W represent batch, channel, height, and width, respectively, and $U = V = A$ represent angular resolution. As shown in Fig. 4, our Distg-Block has a spatial branch, an angular branch and two EPI branches (i.e., horizontal and vertical). In each branch, the input feature is reshaped into a 4-D feature and then convolved by several 2-D convolutions to achieve intra and interview information incorporation.

By adopting Distg-Blocks, our method can incorporate the beneficial spatial and angular information from the input LF to achieve state-of-the-art SR performance. The effectiveness of the Distg-Block for multidegraded LF image SR is validated in Section V-C.

E. Discussion on the Nonblind SR Setting

Recent single image SR methods [31], [52], [56], [57] generally adopt the blind SR settings, i.e., the "groundtruth" degradation is unknown for the SR networks. That is because, compared to nonblind SR methods [49], [50], [51], [58] where the degradation is also required as the input, blind SR is more practical since the real-world degradation is generally difficult to obtain.

However, in this article, we adopt the nonblind SR settings as in [49], and take both degraded LF images and their degradation (blur kernel width and noise level) as inputs of our network. Reasons are in three folds. ***First***, performing nonblind SR helps us to better investigate the impact of input degradation to the SR performance, which has not been studied in LF image SR. Since the kernel width and noise level are independently fed to our network, performing nonblind SR can help us decouple different degradation elements and investigate their influence, respectively, as demonstrated in Section V-D. ***Second***, performing nonblind SR helps us to explore the upper bound of blind SR because the groundtruth degradation information can be used as an accurate prior in nonblind SR. As the first work to achieve LF image SR with multidegradation, one of the major contributions of this article is to break the limitation of single fixed degradation and show the great potential and practical values of multidegraded LF image SR. To this end, nonblind SR is purer and more suitable than blind SR. ***Third***, since the proposed degradation model has only two underdetermined coefficients, we can easily find a proper input degradation by observing the super-resolved images to correct the input degradation, or adopting a grid search strategy [49] to traverse kernel widths and noise levels in a reasonable range, as described in Section V-D2.

V. Experiments

In this section, we first introduce the datasets and implementation details, then compare our network to several state-of-the-art SR methods. Finally, we conduct ablation studies to investigate our design choices and further analyze the impact of the input kernel widths and noise levels.

A. Datasets and Implementation Details

Our method was trained and validated on synthetically degraded LFs generated according to (10), and further tested on real LFs captured by Lytro Illum and Raytrix cameras. For training and validation, three public LF datasets including HCInew [68], HCIold [69], and STFgantry [70] were adopted. The division of training and validation set was kept identical to that in [22], [27], [28], [29]. To test the generalization capability of our method to real-world degradation, three public LF datasets (i.e., EPFL [32],

TABLE I

PSNR AND SSIM RESULTS ACHIEVED BY DIFFERENT METHODS ON THE HCINEW [68], HCIOLD [69], AND STFGANTRY [70] DATASETS UNDER SYNTHETIC DEGRADATION (WITH DIFFERENT BLUR KERNEL WIDTHS AND NOISE LEVELS) FOR 4 × SR. NOTE THAT, THE DEGRADATION DEGENERATES TO THE BICUBIC DOWNSAMPLING DEGRADATION WHEN KERNEL WIDTH AND NOISE LEVEL EQUAL TO 0. BEST RESULTS ARE IN **BOLD FACES** AND THE SECOND BEST RESULTS ARE UNDERLINED

Method	Kernel	HCInew				HCIold				STFgantry			
Noise level		0	15	50	90	0	15	50	90	0	15	50	90
Bicubic	0	27.71/.852	25.90/.789	19.53/.492	14.93/.276	32.58/.934	28.55/.857	20.05/.501	15.12/.257	26.09/.845	24.68/.789	19.18/.516	14.80/.304
DistgSSR		31.38/**.922**	24.88/.722	15.59/.284	10.24/.118	37.56/.973	26.17/.751	15.43/.256	10.10/.092	31.66/.953	24.37/.754	15.53/.319	10.24/.141
LFT		**31.43**/.921	24.99/.729	15.89/.279	10.93/.107	**37.63**/**.974**	26.48/.765	15.96/.258	10.91/.081	**31.80**/**.954**	24.39/.758	15.74/.317	10.93/.136
SRMD		29.55/.886	27.88/.851	25.37/.806	23.76/.780	35.04/.953	31.56/.919	28.26/.883	26.40/.865	28.85/.911	26.73/.869	23.60/.795	21.79/.747
DASR		29.31/.886	27.78/.852	24.10/.785	nan/nan	34.54/.950	31.45/.919	22.70/.829	nan/nan	26.99/.897	26.07/.866	21.92/.768	nan/nan
BSRNet		28.42/.865	24.98/.831	19.32/.748	13.75/.631	32.73/.933	28.22/.895	17.97/.748	13.47/.573	26.55/.880	22.55/.829	17.46/.714	14.39/.618
Real-ESRNet		28.05/.862	26.99/.839	23.65/.789	18.75/.728	31.80/.931	30.11/.905	24.14/.842	17.95/.734	24.78/.871	24.51/.850	19.45/.754	16.31/.690
Ours		30.43/.907	**29.55**/**.886**	**28.23**/**.859**	**27.21**/**.839**	36.44/.967	**34.63**/**.951**	**32.42**/**.929**	**30.88**/**.912**	29.77/.932	**28.62**/**.912**	**26.99**/**.878**	**25.74**/**.848**
Bicubic	1.5	27.02/.836	25.42/.773	19.41/.478	14.89/.266	31.63/.923	28.16/.846	19.99/.491	15.10/.252	25.15/.821	24.00/.764	18.96/.493	14.72/.287
DistgSSR		28.60/.876	24.46/.699	15.60/.273	10.23/.112	33.64/.949	25.97/.739	15.43/.251	10.10/.089	27.16/.883	23.59/.714	15.57/.302	10.27/.131
LFT		28.57/.875	24.60/.708	15.89/.268	10.93/.101	33.62/.949	26.25/.753	15.96/.252	10.92/.079	27.13/.882	23.69/.721	15.70/.295	10.93/.124
SRMD		29.58/.886	27.39/.840	25.01/.798	23.50/.774	35.00/.953	31.02/.912	27.94/.879	26.20/.862	28.87/.910	26.05/.851	23.06/.776	21.40/.732
DASR		29.46/.884	27.34/.840	24.09/.781	nan/nan	34.87/.952	30.95/.911	23.44/.831	nan/nan	27.83/.902	25.84/.850	21.95/.755	nan/nan
BSRNet		28.38/.861	24.79/.824	19.36/.746	13.80/.632	32.77/.932	28.11/.892	18.00/.749	13.48/.574	26.67/.877	22.34/.815	17.39/.706	14.46/.618
Real-ESRNet		28.17/.862	26.68/.830	23.50/.783	18.65/.724	32.11/.932	29.85/.900	24.13/.840	17.91/.731	25.18/.872	24.30/.834	19.41/.741	16.22/.682
Ours		**30.15**/**.900**	**28.98**/**.872**	**27.65**/**.845**	**26.70**/**.826**	**36.10**/**.963**	**33.87**/**.942**	**31.81**/**.920**	**30.36**/**.905**	**29.47**/**.924**	**27.91**/**.894**	**26.25**/**.857**	**25.05**/**.829**
Bicubic	3	25.52/.803	24.32/.741	19.09/.454	14.77/.250	29.59/.898	27.12/.822	19.82/.476	15.04/.243	23.21/.766	22.45/.711	18.41/.450	14.50/.258
DistgSSR		25.79/.811	23.30/.656	15.47/.254	10.21/.104	29.92/.904	25.19/.710	15.38/.241	10.10/.086	23.55/.780	21.83/.639	15.32/.265	10.19/.113
LFT		25.73/.810	23.41/.665	15.75/.248	10.87/.090	29.83/.904	25.42/.724	15.91/.242	10.89/.075	23.47/.779	21.89/.647	15.43/.257	10.81/.104
SRMD		29.20/.876	26.32/.816	24.30/.782	23.04/.763	34.39/.948	29.87/.896	27.36/.871	25.79/.857	28.29/.898	24.51/.807	22.08/.742	20.80/.710
DASR		28.62/.867	26.26/.815	23.70/.767	nan/nan	33.72/.942	29.82/.896	23.75/.829	nan/nan	27.71/.887	24.48/.807	21.50/.723	nan/nan
BSRNet		27.60/.843	24.13/.804	19.33/.740	13.84/.633	31.96/.921	27.72/.883	18.05/.750	13.51/.576	26.05/.849	21.62/.776	17.23/.691	14.50/.618
Real-ESRNet		27.33/.845	25.67/.807	23.04/.769	18.54/.716	31.45/.919	29.11/.889	23.93/.835	17.84/.728	25.24/.856	23.35/.789	19.14/.712	16.08/.670
Ours		**29.43**/**.884**	**27.76**/**.845**	**26.54**/**.821**	**25.74**/**.806**	**35.10**/**.955**	**32.34**/**.924**	**30.54**/**.904**	**29.43**/**.892**	**28.51**/**.904**	**26.22**/**.853**	**24.72**/**.814**	**23.74**/**.788**
Bicubic	4.5	24.36/.779	23.41/.718	18.79/.438	14.65/.240	28.05/.879	26.19/.803	19.63/.465	14.97/.237	21.80/.725	21.26/.672	17.90/.420	14.29/.239
DistgSSR		24.38/.781	22.48/.631	15.33/.242	10.16/.099	28.08/.880	24.50/.690	15.31/.235	10.08/.084	21.83/.728	20.67/.595	15.04/.243	10.12/.103
LFT		24.39/.781	22.57/.640	15.61/.237	10.82/.085	28.08/.880	24.71/.705	15.84/.235	10.85/.072	21.84/.728	20.72/.602	15.14/.233	10.72/.093
SRMD		26.32/.818	25.09/.792	23.65/.769	22.62/.756	30.62/.908	28.61/.882	26.66/.864	25.38/.853	24.34/.780	22.80/.753	21.28/.716	20.37/.697
DASR		25.34/.799	24.89/.788	23.11/.755	nan/nan	29.33/.895	28.39/.880	23.94/.827	nan/nan	22.99/.761	22.65/.749	20.76/.697	nan/nan
BSRNet		26.31/.816	23.40/.784	19.26/.734	13.85/.634	30.35/.902	27.10/.874	18.03/.749	13.51/.577	24.23/.795	20.83/.738	17.06/.680	14.55/.618
Real-ESRNet		26.28/.816	24.69/.787	22.55/.758	18.45/.711	30.04/.900	28.08/.878	23.66/.830	17.77/.726	23.97/.810	22.17/.743	18.90/.693	15.94/.660
Ours		**28.00**/**.854**	**26.55**/**.820**	**25.58**/**.801**	**24.84**/**.788**	**33.39**/**.937**	**30.88**/**.906**	**29.45**/**.890**	**28.52**/**.880**	**26.59**/**.860**	**24.64**/**.808**	**23.30**/**.771**	**22.47**/**.748**

Note: 1) For the methods in [62], [63], we used the models trained with a pixel-wise L1 loss (i.e., BSRNet and Real-ESRNet) for comparison since they can achieve higher PSNR and SSIM values as compared to their GAN-based version (i.e., BSRGAN and Real-ESRGAN). 2) SRMD and our LF-DMnet are non-blind SR methods while DASR, BSRNet and Real-ESRNet are blind SR methods.

INRIA [71], and STFlytro [33]) developed with Lytro cameras and a dataset [72] developed with a Raytrix camera were used as our test sets. Totally 39, 8, and 26 scenes were used for training, validation, and test in this article, respectively.

The LFs in the HCInew [68], HCIold [69], STFgantry [70], EPFL [32], INRIA [71], and STFlytro [33] datasets have an angular resolution of 9 × 9, and the LFs in the Raytrix dataset [72] have an angular resolution of 5 × 5. For LFs with an angular resolution of 9 × 9, we followed the existing works [21], [22], [27], [28], [29] to use the central 5 × 5 SAIs in our experiments. In the training phase, we cropped HR SAIs into patches of size 152 × 152 with a stride of 32, and used the proposed degradation model to synthesize LR SAI patches of size 38 × 38.[3] We followed [31], [52] to set the window size of the isotropic Gaussian kernel to 21 × 21, and followed [49] to randomly sample the kernel width and noise level from range $[0, 4]$ and $[0, 75]$, respectively. Note that, to avoid boundary effect caused by Gaussian filtering, only central 128 × 128 region of the HR patches and their corresponding 32 × 32 LR patches were used for training. We performed random horizontal flipping, vertical flipping, 90° rotation, and RGB channel shuffling to augment the training data by 48×. Note that, the spatial and angular dimension need to be flipped or rotated jointly to maintain LF structures.

Our network was trained using the $L1$ loss and optimized using the Adam method [73] with $\beta_1 = 0.9$, $\beta_2 = 0.999$ and a batch size of 8. Our LF-DMnet was implemented in PyTorch on a PC with two NVidia RTX 2080Ti GPUs. The learning rate was initially set to 2×10^{-4} and decreased by a factor of 0.5 for every 3×10^4 iterations. The training was stopped after 10^5 iterations.

Following [31], [49], [52], we used PSNR and SSIM calculated on the RGB channel images as quantitative metrics for validation. To obtain the metric score (e.g., PSNR) for a dataset with M scenes (each scene has an angular resolution of $A \times A$), we first calculated the metric on $A \times A$ SAIs on each scene separately, then obtained the score for each scene by averaging its A^2 scores, and finally obtained the score for this dataset by averaging the scores of all M scenes.

B. Comparisons With State-of-the-Art Methods

In this section, we compare our method to the following state-of-the-art SR methods.

[3]Following [62], [63], we only consider 4 × SR in this article.

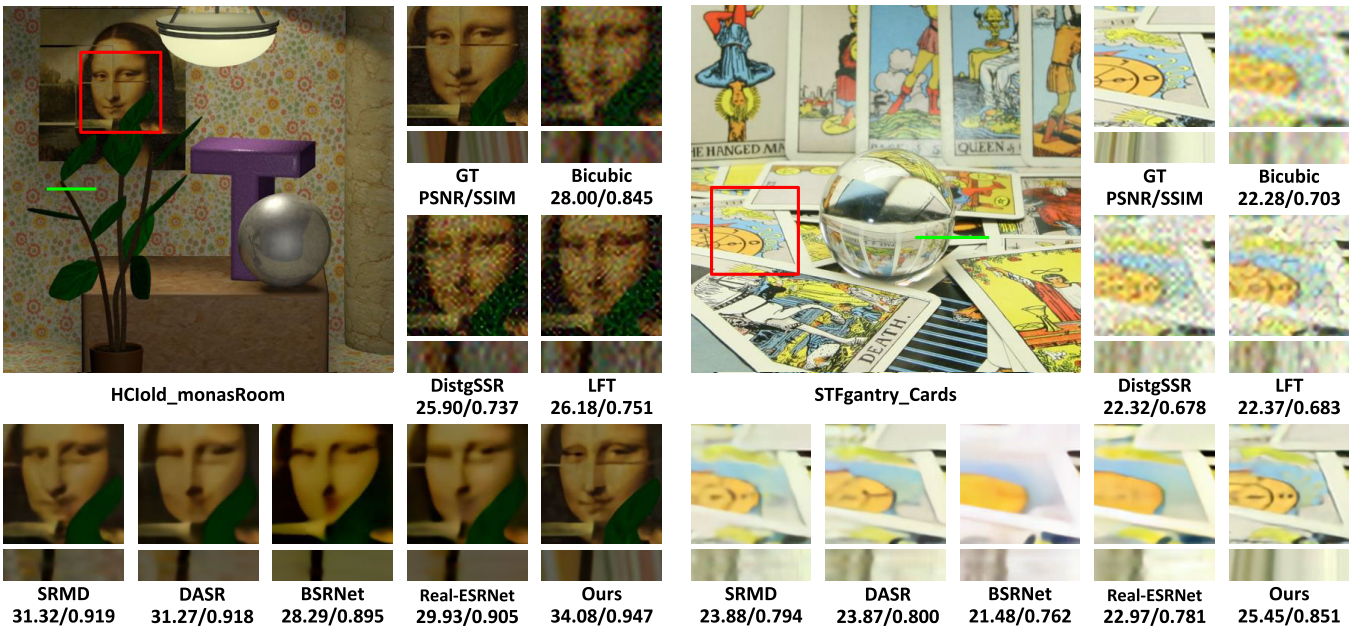

Fig. 5. Visual results achieved by different methods on synthetically degraded LFs (kernel width = 1.5, noise level = 15) for 4 × SR. The super-resolved center view images and horizontal EPIs are shown. The PSNR and SSIM scores on the presented scenes are reported below the zoom-in regions.

1) *DistgSSR [27] and LFT [29]:* Two top-performing LF image SR methods developed on the bicubic downsampling degradation.
2) *SRMD [49]:* A popular nonblind single image SR method developed on isotropic Gaussian blur and Gaussian noise degradation.
3) *DASR [31]:* A state-of-the-art blind single image SR method developed on anisotropic Gaussian blur and Gaussian noise degradation.
4) *BSRGAN [62] and Real-ESRGAN [63]:* Two recent real-world single image SR methods developed on the complex synthetic degradation.

Besides the aforementioned compared methods, we also include bicubic upsampling method to produce baseline results.

1) Results on Synthetically Degraded LFs: Table I shows the quantitative PSNR and SSIM results achieved by different methods under synthetic degradation with different blur and noise levels. It can be observed that DistgSSR and LFT produce the top-2 highest PSNR and SSIM results under the bicubic downsampling degradation (i.e., kernel width = 0, noise level = 0), but suffer from significant performance drop when the kernel width and noise level are larger than zero. This demonstrates that existing LF image SR methods trained on the noise-free bicubic downsampling degradation cannot generalize well to other degradation.

SRMD and DASR achieves much better performance than DistgSSR and LFT on blurry and noisy scenes since these two methods are designed for multidegraded image SR. Note that, SRMD is benefited from the input ground-truth degradation and thus slightly outperforms DASR. It can be also observed that the PSNR and SSIM values produced by BSRNet and Real-ESRNet are lower than SRMD and DASR. That is because, the degradation space in BSRNet and Real-ESRNet are much larger, so that the capability of these two methods in handling specific degradation is less powerful. It is worth noting that these single image SR methods only use spatial context information within single views for SR but overlook the correlations among different views, resulting in inferior SR performance and the angular inconsistency issue (see Section V-B3).

Compared to these state-of-the-art single and LF image SR methods, our LF-DMnet can simultaneously incorporate the complementary angular information and adapt to different degradation, and thus achieves the best PSNR and SSIM results on both in-distribution degradation and out-of-distribution (e.g., *kernel width* = 4.5 or *noise level* = 90) degradation except for the noise-free bicubic downsampling one. The benefits of angular information and degradation adaption are further analyzed in Section V-C. Fig. 5 shows the visual results produced by different methods with blur kernel width and noise level being set to 1.5 and 15, respectively. It can be observed that our LF-DMnet can recover faithful details from the blurry and noisy input LFs.

2) Results on Real LFs: We test the practical values of different SR methods by directly applying them to LFs captured by Lytro and Raytrix cameras. Since the groundtruth HR images of the input LFs are unavailable, we compare the visual results produced by different methods in Figs. 6 and 7. It can be observed that the image quality of the input LFs is low since the bicubically upsampled images are blurry and noisy. DistgSSR and LFT augment the input noise and produce results with artifacts (see Fig. 6) or blurring details (see Fig. 7). This demonstrates that methods developed on the fixed bicubic downsampling degradation cannot handle real-world degradation and thus have limited practical values.

Although SRMD, DASR, BSRGAN, and Real-ESRGAN are specifically designed to handle image SR with multiple

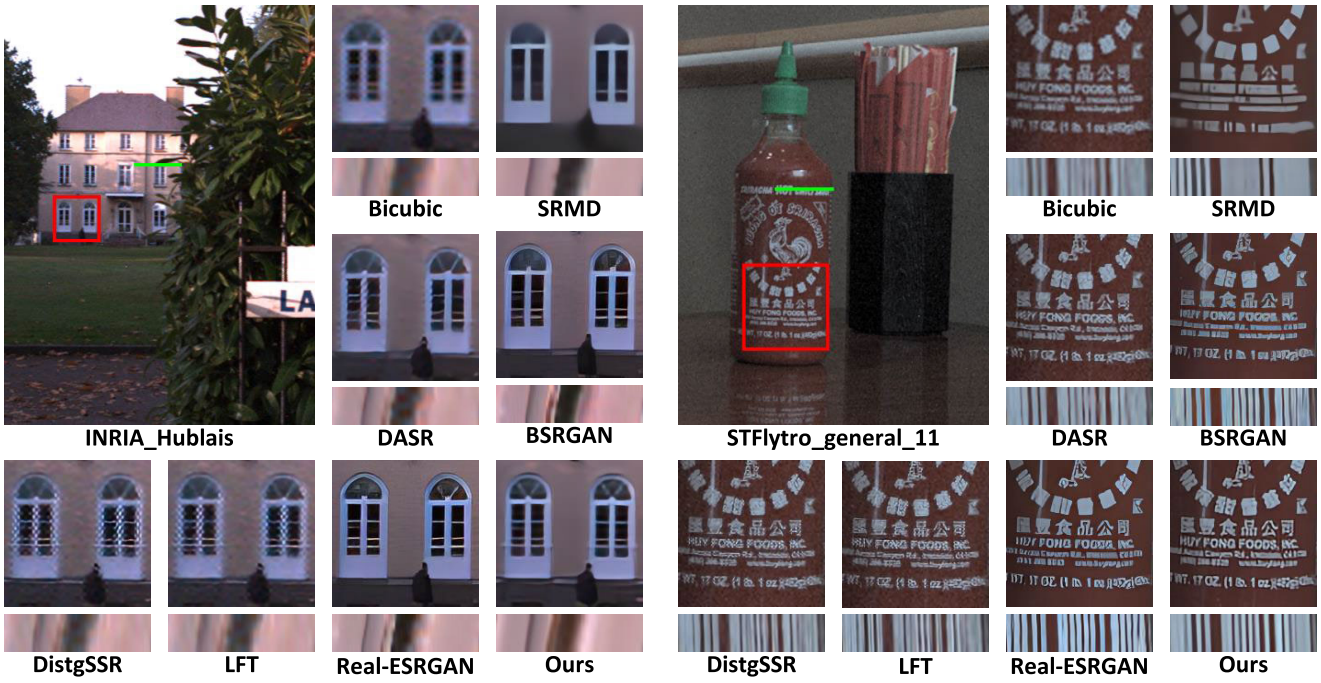

Fig. 6. Visual results achieved by different methods on real LFs captured by Lytro Illum cameras for 4 × SR. Scenes *Hublais* from the INRIA dataset [71] and *general_11* from the STFlytro dataset [33] are used as example scenes for comparison. The super-resolved center view images and horizontal EPIs are shown. For SRMD and our method, the input blur kernel width and noise level are set to 2 and 30, respectively. Groundtruth HR images are unavailable in this case.

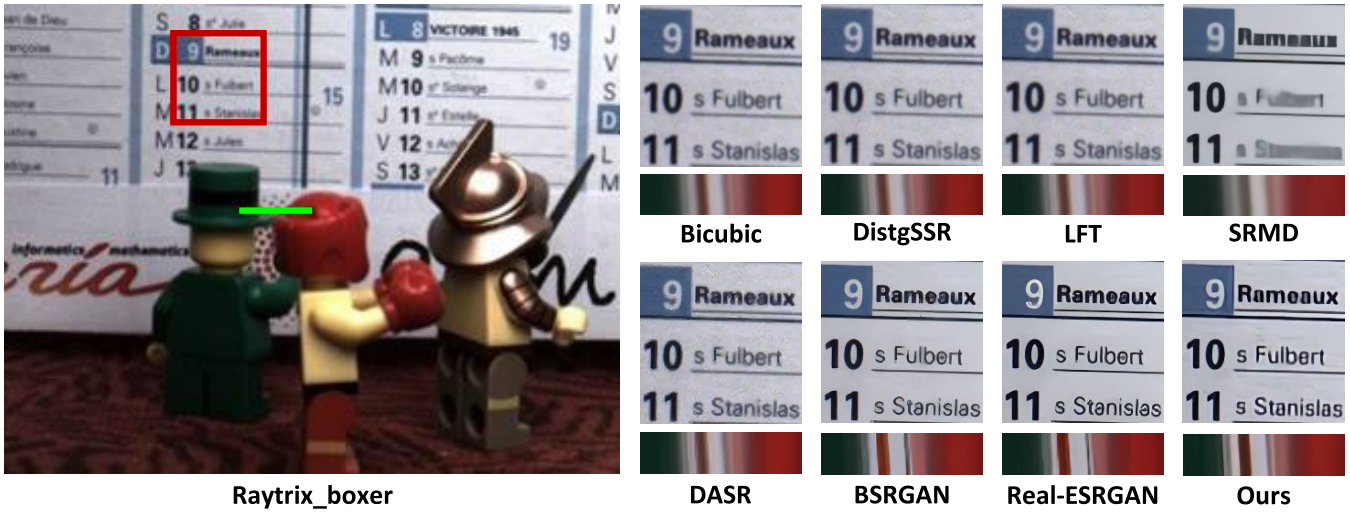

Fig. 7. Visual results achieved by different methods on real LFs captured by a Raytrix camera for 4 × SR. Scenes *boxer* from the dataset in [72] is used as an example scene for comparison. The super-resolved center view images and horizontal EPIs are shown. For SRMD and our method, the input blur kernel width and noise level are set to 4 and 60, respectively. Ground-truth HR images are unavailable in this case.

degradation, these methods do not consider interview correlation and ignore the beneficial angular information. Consequently, these single image SR methods suffer from noise residual (e.g., see the results of DASR in Figs. 6 and 7), oversmoothness (e.g., see the results of SRMD in Figs. 6 and 7), and angular inconsistency (e.g., see the results of BSRGAN and Real-ESRGAN in Fig. 7) issues.

Compared to existing methods, our method achieves the best SR performance on real LFs, i.e., the results produced by our method have finer details (e.g., the words and characters in scene *general_11*) and less artifacts. This demonstrates that our network trained on the proposed degradation model can effectively handle real LF image SR problem. Readers are referred to the videos[4] to view more visual SR results on real LFs.

3) Angular Consistency: Since LF image SR methods are required to preserve the LF parallax structure and generate angular-consistent HR LF images, we evaluate the angular consistency of different SR methods by visualizing their EPI slices. As shown below the zoom-in regions in Figs. 5–7,

[4]https://github.com/YingqianWang/LF-DMnet/blob/main/demo_videos.md

TABLE II
COMPARISONS OF THE NUMBER OF PARAMETERS (#PARAM.), FLOPS, AND RUNNING TIME FOR 4 × SR. NOTE THAT, FLOPS AND RUNNING TIME ARE CALCULATED ON AN INPUT LF WITH AN ANGULAR RESOLUTION OF 5 × 5 AND A SPATIAL RESOLUTION OF 32 × 32. PSNR AND SSIM SCORES ARE AVERAGED OVER NINE DEGRADATION (*Kernel Width* = (0, 1.5, 3), *Noise Level* = (0, 15, 50)) IN TABLE I. BEST RESULTS ARE IN **BOLD FACES**

	#Param.	FLOPs	Time	PSNR/SSIM		
				HCInew	HCIold	STFgantry
SRMD [49]	1.50M	39.76G	0.070s	27.18/0.838	31.16/0.913	25.78/0.840
DASR [31]	5.80M	82.03G	0.051s	26.74/0.831	29.47/0.896	24.92/0.829
BSRNet [62]	16.70M	459.6G	0.119s	24.03/0.807	26.17/0.856	21.98/0.793
Real-ESRNet [63]	16.70M	459.6G	0.119s	25.92/0.821	28.52/0.888	22.82/0.809
DistgSSR [27]	3.53M	65.41G	**0.037s**	22.79/0.611	24.97/0.642	22.06/0.623
LFT [29]	**1.11M**	**29.45G**	0.070s	22.92/0.612	25.23/0.647	22.14/0.623
LF-DMnet (ours)	3.80M	65.93G	0.039s	**28.75/0.869**	**33.69/0.939**	**27.61/0.885**

our LF-DMnet can generate more straight and clear line patterns than other SR methods on both synthetic and real-world degradation, which demonstrates that the LF parallax structure is well preserved by our method. Readers can refer to this video[5] for a visual comparison of angular consistency.

4) Efficiency: We compare our LF-DMnet to existing SR methods in terms of the number of parameters, FLOPs, and running time. As shown in Table II, our LF-DMnet has a moderate model size which is slightly larger than DistgSSR due to the additional KPE branch and the DM-Blocks. Note that, these additional 0.27M parameters only result in a 0.52G and 0.002 s increase in FLOPs and running time, respectively. Compared to DASR, BSRNet (i.e., BSRGAN), and Real-ESRNet (i.e., Real-ESRGAN), our method has significantly smaller model size, lower FLOPs, and shorter running time. These results demonstrate the efficiency of our method.

C. Ablation Study

In this section, we investigate the effectiveness of our proposed modules and design choices by comparing our LF-DMnet with the following variants.

1) *Model 1:* We introduce a baseline model by removing the DM-Block and the angular and EPI branches in the Distg-Block. *Consequently, this variant is equivalent to a plain single image SR network that neither performs degradation modulation nor incorporates angular information.* Note that, we increase the number of convolution layers in this variant to make its model size not smaller than our LF-DMnet.
2) *Model 2:* We investigate the effectiveness of our DM-Conv by replacing it with a depth-wise 3 × 3 convolution and a vanilla 3 × 3 convolution. Distg-Block is maintained in this variant to incorporate angular information. Note that, the KPE module is also removed since vanilla convolutions do not take degradation as their input. *This variant can be considered as an LF image SR method without degradation modulation (e.g., DistgSSR) retrained on our proposed degradation model.*
3) *Model 3:* In this variant, we remove the angular and EPI branches in the Distg-Block and adopt the same strategy as in Model 1 to make the model size of this variant not smaller than our LF-DMnet. *Since this model only incorporates intraview information to achieve degradation-modulated SR, it can be considered as a nonblind single image SR method*, and the benefits of the angular information to real-world LF image SR can be validated.
4) *Model 4:* We modify the KPE module in this variant to investigate the effectiveness of KPE. Specifically, we do not perform isotropic Gaussian kernel reconstruction but directly fed the blur kernel width to a five-layer MLP to generate the blur degradation representation. Consequently, the isotropic Gaussian kernel prior cannot be incorporated by this variant.
5) *Model 5:* In this variant, we remove the degradation-modulating channel attention layer (i.e., DM-CA) from the DM-Block to investigate the benefits of channel-wise degradation modulation.

1) Degradation-Modulating Convolution: As the core component of our LF-DMnet, DM-Conv can adapt image features to the given degradation and thus enhances the capability to handle different degradation. As shown in Table III, without using DM-Conv, Model 2 suffers from a 1.61 dB decrease in average PSNR as compared to LF-DMnet. This is because, different degradation have different spatial characteristics (as analyzed in Section IV-C) and cannot be well handled via fixed convolution kernels. In contrast, our DM-Conv dynamically generates convolutional kernels conditioned on the input degradation to recover the degraded image features, and thus achieves higher PSNR values on a wide range of synthetic degradation. Moreover, we visualize the kernels of our DM-Convs (averaged along the channel dimension) with different input blur and noise levels. As shown in Fig. 8, all the four DM-Convs learn different kernel patterns for different input degradation, and the kernel intensity also varies at different network stages. The above quantitative and visualization results demonstrate the effectiveness of our DM-Conv.

2) Angular Information: The major difference between our LF-DMnet and nonblind single image SR methods (e.g., SRMD) is the incorporation of the angular information. As shown in Table III, when the angular information is not used (i.e., Model 3), the average PSNR value suffers a 2.25 dB drop. This performance gap is also consistent with the gap between SRMD and our method in Table II. This clearly demonstrates that the complementary interview correlation is crucial for real-world LF image SR.

3) Kernel Prior Embedding: It can be observed in Table III that Model 4 without KPE suffers a 0.22 dB decrease in PSNR as compared to our LF-DMnet, and the PSNR drop is more significant on noise-free scenes. That is because, without KPE, our network has to search for the best degradation kernel to recover the degraded image features. Since we adopt the isotropic Gaussian kernel as the blur kernel for synthetic degradation, KPE can help our network to reduce the searching space and thus facilitates our network to learn more accurate kernel representations.

4) Degradation-Modulating Channel Attention: As shown in Table III, when the degradation-modulating channel

[5]https://wyqdatabase.s3.us-west-1.amazonaws.com/LF-DMnet.mp4

TABLE III

PSNR VALUES ACHIEVED BY LF-DMNET AND ITS VARIANTS FOR 4 × SR. HERE, WE REPORT THE NUMBER OF PARAMETERS (#PARAMS.), FLOPS, AND RUNNING TIME OF EACH MODEL FOR EFFICIENCY EVALUATION

Model	DM-Conv	DM-CA	KPE	Ang	#Params.	FLOPs	Time	Noise = 0			Noise = 15			Noise = 50			Average
								σ_b=0	σ_b=1.5	σ_b=3	σ_b=0	σ_b=1.5	σ_b=3	σ_b=0	σ_b=1.5	σ_b=3	
Model 1					3.94M	100.9G	0.029s	27.87	27.72	26.97	26.40	25.71	24.21	23.40	22.85	21.87	25.22
Model 2				✓	3.77M	69.18G	0.038s	28.94	28.28	27.21	28.14	27.31	25.82	26.82	25.99	24.48	26.00
Model 3	✓	✓	✓		4.01M	97.61G	0.030s	27.95	28.00	27.49	26.43	25.79	24.35	23.43	22.92	21.90	25.36
Model 4	✓	✓		✓	3.77M	65.93G	0.038s	29.36	28.91	27.90	28.56	27.77	26.20	26.95	26.14	24.70	27.39
Model 5	✓		✓	✓	3.79M	65.93G	0.037s	29.15	29.29	28.25	28.33	27.85	26.19	26.84	26.16	24.63	27.41
LF-DMnet	✓	✓	✓	✓	3.80M	65.93G	0.039s	**29.77**	**29.47**	**28.51**	**28.62**	**27.91**	**26.22**	**26.99**	**26.25**	**24.72**	**27.61**

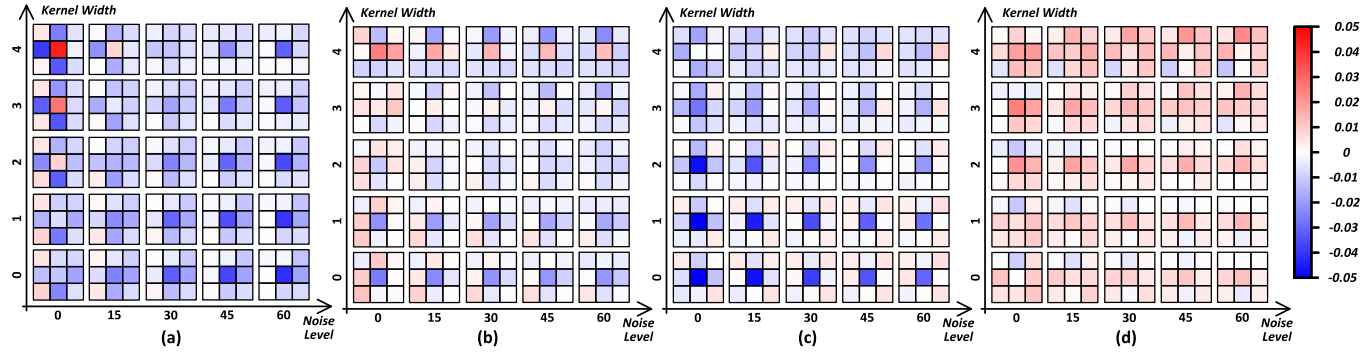

Fig. 8. Kernel visualization of our DM-Convs with different input blur and noise levels. (a) DA-Conv 1. (b) DA-Conv 2. (c) DA-Conv 3. (d) DA-Conv 4.

attention is removed, Model 5 suffers a 0.20 dB decrease in average PSNR as compared to LF-DMnet. This demonstrates the effectiveness of channel-wise degradation modulation. Since our DM-Conv can only adapt to different degradation in the spatial dimension, DM-CA can be used as a complementary part of DM-Conv to enhance its degradation adaptation capability. It is also worth noting that our DM-CA only introduces 0.01 M increase in model size, 2 ms increase in running time, and negligible increase in FLOPs. These results demonstrate the high efficiency of our model design.

D. Degradation Mismatch Analyses

In this section, we first analyze the performance variation of our method with mismatched input and groundtruth synthetic degradation. Then, we apply our LF-DMnet to real LF images and analyze its SR performance with various input blur kernel widths and noise levels.

1) Synthetic Degradation: Since our LF-DMnet is a nonblind SR method, it requires to take the blur kernel and noise level as its input. In the aforementioned experiments with synthetic degradation, we directly use the groundtruth degradation as the input degradation of our network. To investigate the performance of our method when the input degradation mismatches with the groundtruth one, we conduct the following experiments. ***First***, we investigate the performance variation of our LF-DMnet with mismatched blur kernel widths by traversing the groundtruth kernel width B_{gt} and the input kernel width B_{in} from 0 to 3 with a step of 0.3. Fig. 9(a)–(d) visualizes the PSNR values achieved by our method (averaged on the validation scenes) under four different noise levels (i.e., $N_{\text{gt}} = 0, 15, 30, 50$). ***Second***, we investigate the performance variation of our LF-DMnet with mismatched noise levels by traversing the groundtruth noise level N_{gt} and the input noise level N_{in} from 0 to 50 with a step of 5. Fig. 9(e)–(h) visualizes the PSNR values achieved by our method (averaged on the validation scenes) under four different blur kernel widths (i.e., $B_{\text{gt}} = 0, 1, 2, 3$). ***Third***, we investigate the performance variation of our LF-DMnet with simultaneously mismatched blur kernel and noise level by traversing the input blur kernel width B_{in} (from 0 to 3 with a step of 0.3) and the input noise level N_{in} (from 0 to 50 with a step of 5). Fig. 9(i)–(l) visualizes the PSNR values achieved by our method (averaged on the validation scenes) under four representative degradation settings including $(B_{\text{gt}}, N_{\text{gt}}) = (0, 0), (3, 0), (1.5, 15)$, and $(0, 30)$.

From Fig. 9, we can draw the following conclusions.

1) Best SR performance can be achieved when the input degradation matches the groundtruth one.
2) The performance variation caused by blur mismatch is more significant than that caused by noise mismatch.
3) When $B_{\text{in}} \neq B_{\text{gt}}$, $B_{\text{in}} > B_{\text{gt}}$ leads to much more significant performance degradation than $B_{\text{in}} < B_{\text{gt}}$.
4) As the noise level increases, the PSNR variation caused by the blur kernel mismatch is reduced.

2) Real-World Degradation: To investigate the influence of the input kernel widths and noise levels to the SR performance under real-world degradation, we directly apply our LF-DMnet to the LFs captured by Lytro and Raytrix cameras, and traverse the input blur kernel width (from 0 to 3 with a step of 1) and the input noise level (from 0 to 60 with a step of 15). Since both the groundtruth HR images and their degradation are unavailable, we evaluate the performance of our method by visually comparing its SR results. Fig. 10 shows the 4 × SR results achieved by our method with varied input degradation, from which we can obtain the following conclusions.

1) A large input kernel width can enhance the local contrast and sharpens edges and textures, but an over-large

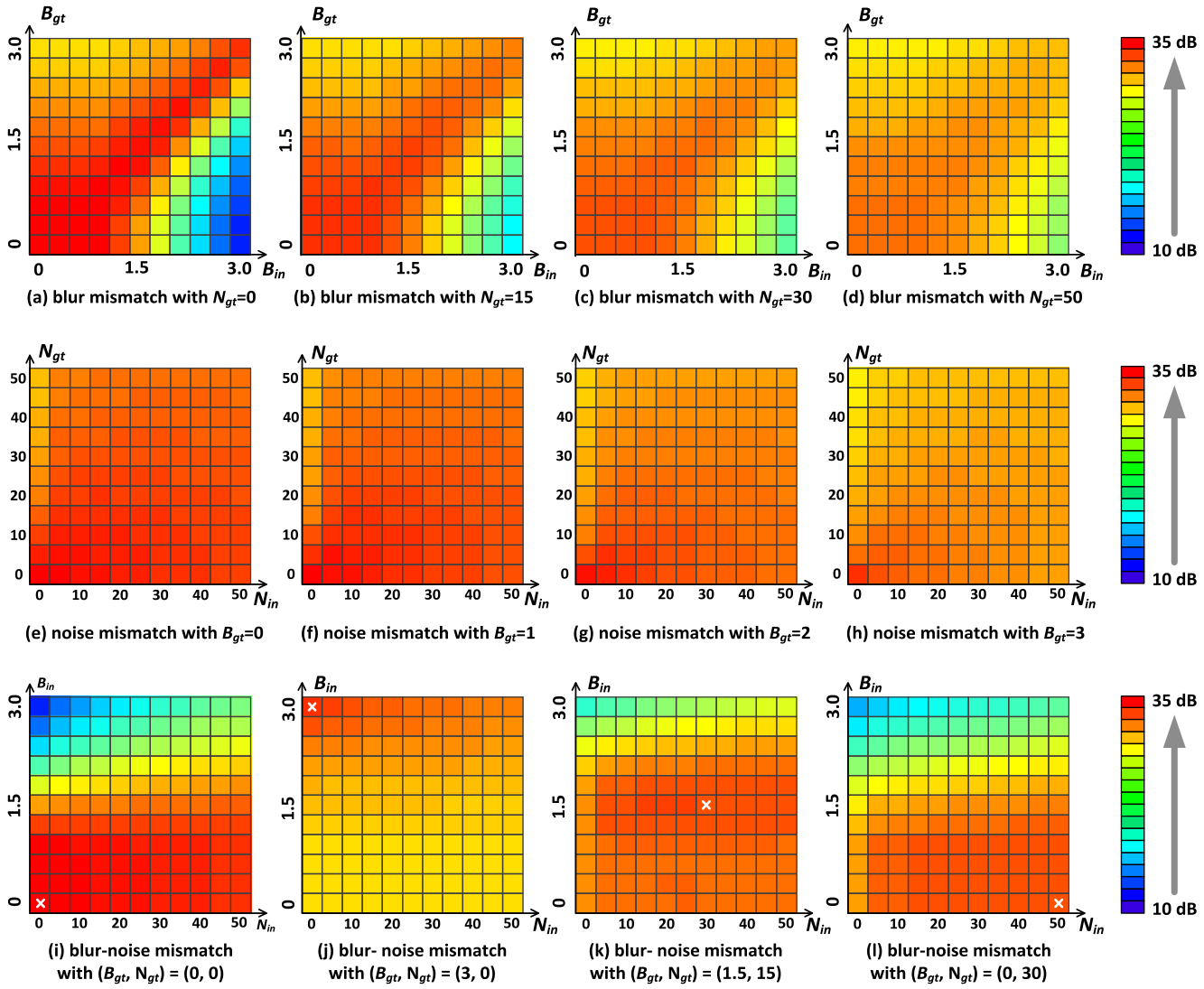

Fig. 9. Visualization of the performance variation of our method with mismatched degradation. (a)–(d) PSNR values achieved with mismatched blur kernel widths under different noise levels. (e)–(h) PSNR values achieved with mismatched noise level under different blurs. (i)–(l) PSNR values achieved with simultaneously mismatched blurs and noise levels under four representative degradation settings (marked by white cross).

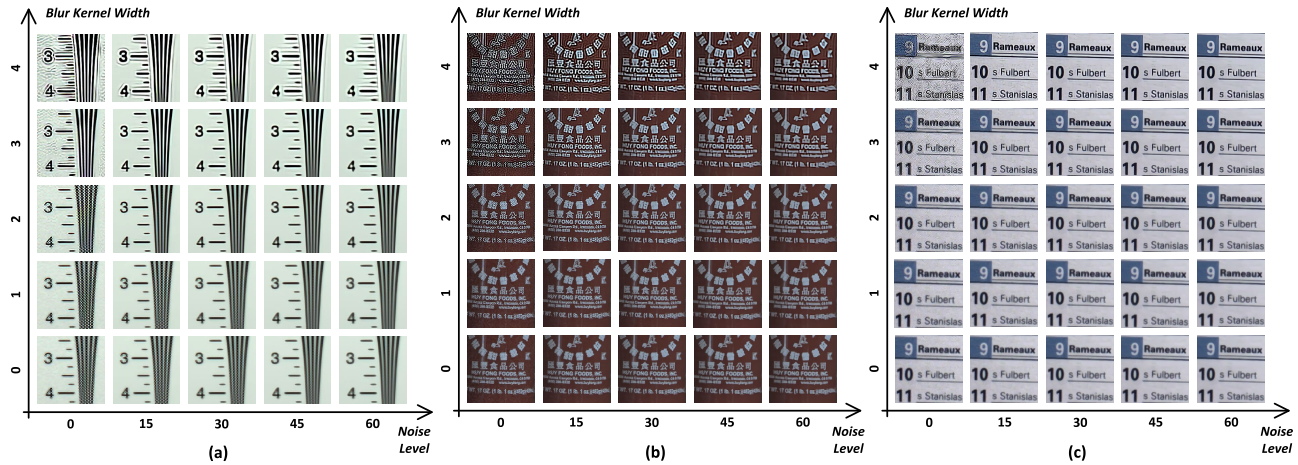

Fig. 10. Visual results achieved by our method on real LF images with different blur kernel width and noise levels. Three scenes from the EPFL [32], STFlytro [33], and Raytrix [72] datasets are used as examples for illustration. (a) EPFL_ISO_Chart. (b) STFlytro_general_11. (c) Raytrix_boxer.

kernel width introduces ringing artifacts to the result images.

2) A large input noise level can enhance the local smoothness and helps to alleviate the artifacts, but an

over-large input noise level makes the result images blurring.

3) Our LF-DMnet can achieve better SR performance on Lytro LFs by setting kernel width and noise level to 2 and 30, respectively, and can achieve better SR performance on Raytrix LFs by setting kernel width and noise level to 4 and 60, respectively.

Readers can further refer to our interactive online demo[6] to view the influence of input degradation to the SR results.

VI. Conclusion and Discussion

In this article, we achieve real-world LF image SR via degradation modulation. We developed an LF degradation model based on the camera imaging process, and proposed an LF-DMnet that can modulate degradation priors into the SR process. Experimental results show that our method can produce visually pleasant and angular consistent SR results on real-world LF images. Through extensive ablation studies and model analyses, we validated the effectiveness of our designs and obtained a series of insightful observations.

It is worth noting that, although our LF-DMnet achieves significantly improved performance than existing methods on real-world LF image SR, it is sensitive to the input degradation and requires accurate degradation estimation. When the input blur kernel widths and noise levels mismatch with the real ones, our method will produce images with artifacts or oversmoothness. Moreover, due to the nonblind setting in our method, when applying our method to a novel LF camera with unknown degradation, we need to first "measure" the PSF and the noise level of this camera, which is user-unfriendly and not practical enough. In the future, we will study the more challenging blind LF image SR problem, and try to design a more practical method for real-world LF image SR. We believe that our LF-DMnet will serve as a fundamental work and can inspire more researchers to focus on real-world LF image SR.

References

[1] S. S. Jayaweera, C. U. S. Edussooriya, C. Wijenayake, P. Agathoklis, and L. T. Bruton, "Multi-volumetric refocusing of light fields," *IEEE Signal Process. Lett.*, vol. 28, pp. 31–35, 2021.

[2] Y. Wang, L. Wang, Z. Liang, J. Yang, W. An, and Y. Guo, "Occlusion-aware cost constructor for light field depth estimation," in *Proc. IEEE/CVF Conf. Comput. Vis. Pattern Recognit. (CVPR)*, Jun. 2022, pp. 19809–19818.

[3] C. Shin, H.-G. Jeon, Y. Yoon, I. S. Kweon, and S. J. Kim, "EPINET: A fully-convolutional neural network using epipolar geometry for depth from light field images," in *Proc. IEEE/CVF Conf. Comput. Vis. Pattern Recognit.*, Jun. 2018, pp. 4748–4757.

[4] W. Zhou, L. Lin, Y. Hong, Q. Li, X. Shen, and E. E. Kuruoglu, "Beyond photometric consistency: Geometry-based occlusion-aware unsupervised light field disparity estimation," *IEEE Trans. Neural Netw. Learn. Syst.*, early access, Jul. 4, 2023, doi: 10.1109/TNNLS.2023.3289056.

[5] C. Zhu, H. Zhang, W. Chen, M. Tan, and Q. Liu, "An occlusion compensation learning framework for improving the rendering quality of light field," *IEEE Trans. Neural Netw. Learn. Syst.*, vol. 32, no. 12, pp. 5738–5752, Dec. 2021.

[6] G. Wu, Y. Liu, L. Fang, and T. Chai, "Revisiting light field rendering with deep anti-aliasing neural network," *IEEE Trans. Pattern Anal. Mach. Intell.*, vol. 44, no. 9, pp. 5430–5444, Sep. 2022.

[7] G. Wu, Y. Wang, Y. Liu, L. Fang, and T. Chai, "Spatial-angular attention network for light field reconstruction," *IEEE Trans. Image Process.*, vol. 30, pp. 8999–9013, 2021.

[6]https://yingqianwang.github.io/LF-DMnet/

[8] M. Zhang, Q. Wu, J. Guo, Y. Li, and X. Gao, "Heat transfer-inspired network for image super-resolution reconstruction," *IEEE Trans. Neural Netw. Learn. Syst.*, vol. 35, no. 2, pp. 1810–1820, Feb. 2024.

[9] C. Tian, Y. Zhang, W. Zuo, C.-W. Lin, D. Zhang, and Y. Yuan, "A heterogeneous group CNN for image super-resolution," *IEEE Trans. Neural Netw. Learn. Syst.*, early access, Oct. 13, 2022, doi: 10.1109/TNNLS.2022.3210433.

[10] X. Hu, Z. Zhang, C. Shan, Z. Wang, L. Wang, and T. Tan, "Meta-USR: A unified super-resolution network for multiple degradation parameters," *IEEE Trans. Neural Netw. Learn. Syst.*, vol. 32, no. 9, pp. 4151–4165, Sep. 2021.

[11] K. Li, "Local means binary networks for image super-resolution," *IEEE Trans. Neural Netw. Learn. Syst.*, early access, Oct. 21, 2022, doi: 10.1109/TNNLS.2022.3212827.

[12] G. Wu, J. Jiang, and X. Liu, "A practical contrastive learning framework for single-image super-resolution," *IEEE Trans. Neural Netw. Learn. Syst.*, early access, Jul. 10, 2023, doi: 10.1109/TNNLS.2023.3290038.

[13] Y. Yoon, H.-G. Jeon, D. Yoo, J.-Y. Lee, and I. S. Kweon, "Learning a deep convolutional network for light-field image super-resolution," in *Proc. IEEE Int. Conf. Comput. Vis. Workshop (ICCVW)*, Dec. 2015, pp. 24–32.

[14] Y. Yoon, H.-G. Jeon, D. Yoo, J.-Y. Lee, and I. S. Kweon, "Light-field image super-resolution using convolutional neural network," *IEEE Signal Process. Lett.*, vol. 24, no. 6, pp. 848–852, Jun. 2017.

[15] Y. Wang, F. Liu, K. Zhang, G. Hou, Z. Sun, and T. Tan, "LFNet: A novel bidirectional recurrent convolutional neural network for light-field image super-resolution," *IEEE Trans. Image Process.*, vol. 27, pp. 4274–4286, 2018.

[16] H. W. F. Yeung, J. Hou, X. Chen, J. Chen, Z. Chen, and Y. Y. Chung, "Light field spatial super-resolution using deep efficient spatial-angular separable convolution," *IEEE Trans. Image Process.*, vol. 28, no. 5, pp. 2319–2330, May 2019.

[17] N. Meng, H. K.-H. So, X. Sun, and E. Y. Lam, "High-dimensional dense residual convolutional neural network for light field reconstruction," *IEEE Trans. Pattern Anal. Mach. Intell.*, vol. 43, no. 3, pp. 873–886, Mar. 2021.

[18] Z. Cheng, Z. Xiong, and D. Liu, "Light field super-resolution by jointly exploiting internal and external similarities," *IEEE Trans. Circuits Syst. Video Technol.*, vol. 30, no. 8, pp. 2604–2616, Aug. 2020.

[19] S. Zhang, Y. Lin, and H. Sheng, "Residual networks for light field image super-resolution," in *Proc. IEEE/CVF Conf. Comput. Vis. Pattern Recognit. (CVPR)*, Jun. 2019, pp. 11046–11055.

[20] J. Jin, J. Hou, J. Chen, and S. Kwong, "Light field spatial super-resolution via deep combinatorial geometry embedding and structural consistency regularization," in *Proc. IEEE/CVF Conf. Comput. Vis. Pattern Recognit. (CVPR)*, Jun. 2020, pp. 2260–2269.

[21] Y. Wang, L. Wang, J. Yang, W. An, J. Yu, and Y. Guo, "Spatial-angular interaction for light field image super-resolution," in *Proc. Eur. Conf. Comput. Vis. (ECCV)*, 2020, pp. 290–308.

[22] Y. Wang et al., "Light field image super-resolution using deformable convolution," *IEEE Trans. Image Process.*, vol. 30, pp. 1057–1071, 2021.

[23] S. Zhang, S. Chang, and Y. Lin, "End-to-end light field spatial super-resolution network using multiple epipolar geometry," *IEEE Trans. Image Process.*, vol. 30, pp. 5956–5968, 2021.

[24] Z. Cheng, Z. Xiong, C. Chen, D. Liu, and Z.-J. Zha, "Light field super-resolution with zero-shot learning," in *Proc. IEEE Conf. Comput. Vis. Pattern Recog.*, Jun. 2021, pp. 10010–10019.

[25] Z. Cheng, Y. Liu, and Z. Xiong, "Spatial-angular versatile convolution for light field reconstruction," *IEEE Trans. Comput. Imag.*, vol. 8, pp. 1131–1144, 2022.

[26] K. Ko, Y. J. Koh, S. Chang, and C. Kim, "Light field super-resolution via adaptive feature remixing," *IEEE Trans. Image Process.*, vol. 30, pp. 4114–4128, 2021.

[27] Y. Wang et al., "Disentangling light fields for super-resolution and disparity estimation," *IEEE Trans. Pattern Anal. Mach. Intell.*, vol. 45, no. 1, pp. 425–443, Jan. 2023.

[28] S. Wang, T. Zhou, Y. Lu, and H. Di, "Detail-preserving transformer for light field image super-resolution," in *Proc. AAAI Conf. Artif. Intell. (AAAI)*, 2022, pp. 2522–2530.

[29] Z. Liang, Y. Wang, L. Wang, J. Yang, and S. Zhou, "Light field image super-resolution with transformers," *IEEE Signal Process. Lett.*, vol. 29, pp. 563–567, 2022.

[30] Z. Liang, Y. Wang, L. Wang, J. Yang, S. Zhou, and Y. Guo, "Learning non-local spatial-angular correlation for light field image super-resolution," in *Proc. IEEE/CVF Int. Conf. Comput. Vis. (ICCV)*, Oct. 2023, pp. 12377–12386.

[31] L. Wang et al., "Unsupervised degradation representation learning for blind super-resolution," in *Proc. IEEE/CVF Conf. Comput. Vis. Pattern Recognit. (CVPR)*, Jun. 2021, pp. 10576–10585.

[32] M. Rerabek and T. Ebrahimi, "New light field image dataset," in *Proc. Int. Conf. Quality Multimedia Exper. (QoMEX)*, 2016.

[33] A. S. Raj, M. Lowney, R. Shah, and G. Wetzstein, "Stanford lytro light field archive," 2016.

[34] C. Dong, C. C. Loy, K. He, and X. Tang, "Learning a deep convolutional network for image super-resolution," in *Proc. Eur. Conf. Comput. Vis.*, 2014, pp. 184–199.

[35] R. Timofte, V. De, and L. V. Gool, "Anchored neighborhood regression for fast example-based super-resolution," in *Proc. IEEE Int. Conf. Comput. Vis.*, Dec. 2013, pp. 1920–1927.

[36] R. Timofte, V. De Smet, and L. Van Gool, "A+: Adjusted anchored neighborhood regression for fast super-resolution," in *Proc. Asian Conf. Comput. Vis.*, Cham, Switzerland: Springer, 2014, pp. 111–126.

[37] J. Yang, J. Wright, T. S. Huang, and Y. Ma, "Image super-resolution via sparse representation," *IEEE Trans. Image Process.*, vol. 19, no. 11, pp. 2861–2873, Nov. 2010.

[38] K. I. Kim and Y. Kwon, "Single-image super-resolution using sparse regression and natural image prior," *IEEE Trans. Pattern Anal. Mach. Intell.*, vol. 32, no. 6, pp. 1127–1133, Jun. 2010.

[39] J. Kim, J. K. Lee, and K. M. Lee, "Accurate image super-resolution using very deep convolutional networks," in *Proc. IEEE Conf. Comput. Vis. Pattern Recognit. (CVPR)*, Jun. 2016, pp. 1646–1654.

[40] B. Lim, S. Son, H. Kim, S. Nah, and K. M. Lee, "Enhanced deep residual networks for single image super-resolution," in *Proc. IEEE Conf. Comput. Vis. Pattern Recognit. Workshops (CVPRW)*, Jul. 2017, pp. 136–144.

[41] Y. Zhang, Y. Tian, Y. Kong, B. Zhong, and Y. Fu, "Residual dense network for image super-resolution," in *Proc. IEEE/CVF Conf. Comput. Vis. Pattern Recognit.*, Jun. 2018, pp. 2472–2481.

[42] Y. Zhang, K. Li, K. Li, L. Wang, B. Zhong, and Y. Fu, "Image super-resolution using very deep residual channel attention networks," in *Proc. Eur. Conf. Comput. Vis. (ECCV)*, Sep. 2018, pp. 286–301.

[43] Y. Zhang, K. Li, K. Li, B. Zhong, and Y. Fu, "Residual non-local attention networks for image restoration," in *Proc. Int. Conf. Learn. Represent. (ICLR)*, 2019.

[44] H. Wang, D. Su, C. Liu, L. Jin, X. Sun, and X. Peng, "Deformable non-local network for video super-resolution," *IEEE Access*, vol. 7, pp. 177734–177744, 2019.

[45] Y. Zhang, D. Wei, C. Qin, H. Wang, H. Pfister, and Y. Fu, "Context reasoning attention network for image super-resolution," in *Proc. IEEE/CVF Int. Conf. Comput. Vis. (ICCV)*, Oct. 2021, pp. 4278–4287.

[46] J. Liang, J. Cao, G. Sun, K. Zhang, L. Van Gool, and R. Timofte, "Swinir: Image restoration using Swin transformer," in *Proc. IEEE/CVF Int. Conf. Comput. Vis. (ICCV) Workshops*, Oct. 2021, pp. 1833–1844.

[47] Z. Lu, J. Li, H. Liu, C. Huang, L. Zhang, and T. Zeng, "Transformer for single image super-resolution," in *Proc. IEEE/CVF Conf. Comput. Vis. Pattern Recognit. Workshops (CVPRW)*, Jun. 2022, pp. 456–465.

[48] A. Liu, Y. Liu, J. Gu, Y. Qiao, and C. Dong, "Blind image super-resolution: A survey and beyond," 2021, *arXiv:2107.03055*.

[49] K. Zhang, W. Zuo, and L. Zhang, "Learning a single convolutional super-resolution network for multiple degradations," in *Proc. IEEE/CVF Conf. Comput. Vis. Pattern Recognit.*, Jun. 2018, pp. 3262–3271.

[50] Y.-S. Xu, S. R. Tseng, Y. Tseng, H.-K. Kuo, and Y.-M. Tsai, "Unified dynamic convolutional network for super-resolution with variational degradations," in *Proc. IEEE/CVF Conf. Comput. Vis. Pattern Recognit. (CVPR)*, Jun. 2020, pp. 12493–12502.

[51] K. Zhang, L. Van Gool, and R. Timofte, "Deep unfolding network for image super-resolution," in *Proc. IEEE/CVF Conf. Comput. Vis. Pattern Recognit. (CVPR)*, Jun. 2020, pp. 3217–3226.

[52] J. Gu, H. Lu, W. Zuo, and C. Dong, "Blind super-resolution with iterative kernel correction," in *Proc. IEEE/CVF Conf. Comput. Vis. Pattern Recognit. (CVPR)*, Jun. 2019, pp. 1604–1613.

[53] J. Dai et al., "Deformable convolutional networks," in *Proc. IEEE Int. Conf. Comput. Vis. (ICCV)*, Oct. 2017, pp. 764–773.

[54] X. Zhu, H. Hu, S. Lin, and J. Dai, "Deformable ConvNets v2: More deformable, better results," in *Proc. IEEE/CVF Conf. Comput. Vis. Pattern Recognit. (CVPR)*, Jun. 2019, pp. 9308–9316.

[55] M. Levoy and P. Hanrahan, "Light field rendering," in *Proc. 23rd Annu. Conf. Comput. Graph. Interact. Techn.*, Aug. 1996, pp. 31–42.

[56] J. Liang, K. Zhang, S. Gu, L. V. Gool, and R. Timofte, "Flow-based kernel prior with application to blind super-resolution," in *Proc. IEEE/CVF Conf. Comput. Vis. Pattern Recognit. (CVPR)*, Jun. 2021, pp. 10596–10605.

[57] J. Liang, G. Sun, K. Zhang, L. V. Gool, and R. Timofte, "Mutual affine network for spatially variant kernel estimation in blind image super-resolution," in *Proc. IEEE/CVF Int. Conf. Comput. Vis. (ICCV)*, Oct. 2021, pp. 4076–4085.

[58] K. Zhang, W. Zuo, and L. Zhang, "Deep plug-and-play super-resolution for arbitrary blur kernels," in *Proc. IEEE/CVF Conf. Comput. Vis. Pattern Recognit. (CVPR)*, Jun. 2019, pp. 1671–1681.

[59] P. P. Srinivasan, R. Ng, and R. Ramamoorthi, "Light field blind motion deblurring," in *Proc. IEEE Conf. Comput. Vis. Pattern Recognit. (CVPR)*, Jul. 2017, pp. 2354–2362.

[60] D. Lee, H. Park, I. K. Park, and K. M. Lee, "Joint blind motion deblurring and depth estimation of light field," in *Proc. Eur. Conf. Comput. Vis. (ECCV)*, Sep. 2018, pp. 288–303.

[61] M. R. M. Mohan and A. N. Rajagopalan, "Divide and conquer for full-resolution light field deblurring," in *Proc. IEEE/CVF Conf. Comput. Vis. Pattern Recognit.*, Jun. 2018, pp. 6421–6429.

[62] K. Zhang, J. Liang, L. Van Gool, and R. Timofte, "Designing a practical degradation model for deep blind image super-resolution," in *Proc. IEEE/CVF Int. Conf. Comput. Vis. (ICCV)*, Oct. 2021, pp. 4791–4800.

[63] X. Wang, L. Xie, C. Dong, and Y. Shan, "Real-ESRGAN: Training real-world blind super-resolution with pure synthetic data," in *Proc. IEEE/CVF Int. Conf. Comput. Vis. Workshops (ICCVW)*, Oct. 2021, pp. 1905–1914.

[64] E. Agustsson and R. Timofte, "NTIRE 2017 challenge on single image super-resolution: Dataset and study," in *Proc. IEEE Conf. Comput. Vis. Pattern Recognit. Workshops*, Jul. 2017, pp. 126–135.

[65] R. Timofte et al., "NTIRE 2017 challenge on single image super-resolution: Methods and results," in *Proc. IEEE Conf. Comput. Vis. Pattern Recognit. Workshops*, Jul. 2017, pp. 114–125.

[66] X. Wang, K. Yu, C. Dong, and C. Change Loy, "Recovering realistic texture in image super-resolution by deep spatial feature transform," in *Proc. IEEE/CVF Conf. Comput. Vis. Pattern Recognit.*, Jun. 2018, pp. 606–615.

[67] K. Ma et al., "Waterloo exploration database: New challenges for image quality assessment models," *IEEE Trans. Image Process.*, vol. 26, no. 2, pp. 1004–1016, Feb. 2017.

[68] K. Honauer, O. Johannsen, D. Kondermann, and B. Goldluecke, "A dataset and evaluation methodology for depth estimation on 4D light fields," in *Proc. Asian Conf. Comput. Vis.*, 2016, pp. 19–34.

[69] S. Wanner, S. Meister, and B. Goldluecke, "Datasets and benchmarks for densely sampled 4D light fields," in *Proc. VMV*, vol. 13, 2013, pp. 225–226.

[70] V. Vaish and A. Adams, "The (new) Stanford light field archive," Comput. Graph. Lab., Stanford Univ., Stanford, CA, USA, 2008, vol. 6, no. 7. [Online]. Available: http://lightfield.stanford.edu/lfs.html

[71] M. Le Pendu, X. Jiang, and C. Guillemot, "Light field inpainting propagation via low rank matrix completion," *IEEE Trans. Image Process.*, vol. 27, no. 4, pp. 1981–1993, Apr. 2018.

[72] L. Guillo, X. Jiang, G. Lafruit, and C. Guillemot, *Light Field Video Dataset Captured by a R8 Raytrix Camera (With Disparity Maps)*, ISO/IEC JTC1/SC29/WG1 & WG11, Int. Organisation for Standardisation, 2018.

[73] D. P. Kingma and J. Ba, "Adam: A method for stochastic optimization," in *Proc. Int. Conf. Learn. Represent. (ICLR)*, 2015.

Yingqian Wang received the B.E. degree in electrical engineering from Shandong University, Jinan, China, in 2016, and the master's and Ph.D. degrees in information and communication engineering from the National University of Defense Technology (NUDT), Changsha, China, in 2018 and 2023, respectively.

He is currently an Assistant Professor with the College of Electronic Science and Technology, NUDT. His research interests focus on optical imaging and detection, particularly on light field imaging, image super-resolution, and infrared small target detection.

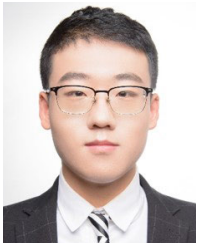

Zhengyu Liang received the B.E. degree from Xidian University, Xi'an, China, in 2019, and the M.E. degree in information and communication engineering from the National University of Defense Technology (NUDT), Changsha, China, in 2021, where he is currently pursuing the Ph.D. degree with the College of Electronic Science and Technology.

His current research interests mainly focus on low-level vision, particularly on light-field image processing and image super-resolution.

Longguang Wang received the B.E. degree in electrical engineering from Shandong University (SDU), Jinan, China, in 2015, and the Ph.D. degree in information and communication engineering from the National University of Defense Technology (NUDT), Changsha, China, in 2022.

His current research interests include low-level vision and 3-D vision.

Jungang Yang received the B.E. and Ph.D. degrees from the National University of Defense Technology (NUDT), Changsha, China, in 2007 and 2013, respectively.

He was a Visiting Ph.D. Student with the University of Edinburgh, Edinburgh, U.K., from 2011 to 2012. He is currently an Associate Professor with the College of Electronic Science, NUDT. His research interests include computational imaging, image processing, compressive sensing, and sparse representation.

Dr. Yang received the New Scholar Award of Chinese Ministry of Education in 2012, the Youth Innovation Award, and the Youth Outstanding Talent of NUDT in 2016.

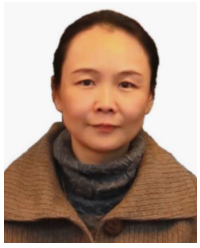

Wei An received the Ph.D. degree from the National University of Defense Technology (NUDT), Changsha, China, in 1999.

She was a Senior Visiting Scholar with the University of Southampton, Southampton, U.K., in 2016. She is currently a Professor with the College of Electronic Science and Technology, NUDT. She has authored or coauthored more than 100 journal and conference publications. Her current research interests include signal processing and image processing.

Yulan Guo (Senior Member, IEEE) received the B.E. and Ph.D. degrees from the National University of Defense Technology (NUDT), Changsha, China, in 2008 and 2015, respectively. He is currently an Associate Professor.

He has authored more than 100 articles at highly referred journals and conferences. His current research interests focus on 3-D vision, particularly on 3-D feature learning, 3-D modeling, 3-D object recognition, and scene understanding.

Dr. Guo served as an Associate Editor for IEEE TRANSACTIONS ON IMAGE PROCESSING, a Guest Editor for IEEE TRANSACTIONS ON PATTERN ANALYSIS AND MACHINE INTELLIGENCE, and an Area Chair for CVPR 2021, ICCV 2021, and ACM Multimedia 2021. He organized several tutorials and workshops in prestigious conferences, such as CVPR 2016, CVPR 2019, ICCV 2021, and 3DV 2021. He is a Senior Member of ACM.